Ultraviolet–visible–near-infrared optical properties of amyloid fibrils shed light on amyloidogenesis

18 authors, including:

Jonathan Pansieri
Oxford University Hospitals NHS Trust
24 PUBLICATIONS   233 CITATIONS

SEE PROFILE

Véronique Josserand
Floralis
147 PUBLICATIONS   3,751 CITATIONS

SEE PROFILE

Anaëlle Rongier
Atomic Energy and Alternative Energies Commission
7 PUBLICATIONS   99 CITATIONS

SEE PROFILE

Daniel Imbert
Atomic Energy and Alternative Energies Commission
84 PUBLICATIONS   3,870 CITATIONS

SEE PROFILE

Some of the authors of this publication are also working on these related projects:

Project   Psoriasis & Cdk-cyclins View project

Project   functionalised nanoparticles for amyloidosis diagnostic View project

Ultraviolet–visible–near-infrared optical properties of amyloid fibrils shed light on amyloidogenesis

Jonathan Pansieri [1,11], Véronique Josserand [2], Sun-Jae Lee [1,3], Anaëlle Rongier [1,3], Daniel Imbert [3], Marcelle Moulin Sallanon [4,5], Enikö Kövari [6], Thomas G. Dane [7], Charlotte Vendrely [8,9], Odette Chaix-Pluchery [9], Mélanie Guidetti [2], Julien Vollaire [2], Arnold Fertin [10], Yves Usson [10], Patrice Rannou [3], Jean-Luc Coll [2], Christel Marquette [1] and Vincent Forge [1]*

Amyloid fibres attract considerable interest due to their biological role in neurodegenerative diseases and their potential as functional biomaterials. Here, we describe an intrinsic signal of amyloid fibres in the near-infrared range. When combined with their recently reported blue luminescence, it paves the way towards new blueprints for the label-free detection of amyloid deposits in in vitro and in vivo contexts. The blue luminescence allows for staining-free characterization of amyloid deposits in human samples. The near-infrared signal offers promising prospects for innovative diagnostic strategies for neurodegenerative diseases—to improve medical care and for the development of new therapies. As a proof of concept, we demonstrate direct detection of amyloid deposits within brains of living, aged mice with Alzheimer's disease using non-invasive and contrast-agent-free imaging. Ultraviolet–visible–near-infrared optical properties of amyloids open new research avenues for amyloidosis as well as for next-generation biophotonic devices.

Amyloid fibres result from the self-assembly of polypeptides into high-aspect-ratio nanowires[1–3]. These supramolecular protein assemblies are studied for their biological roles[1,2] and for their potential as new biomaterials[4–6]. They have been widely studied within the context of neurodegenerative diseases, such as Alzheimer's disease and Parkinson's disease, because they are the constituents of amyloid deposits, a hallmark of these disorders[7,8]. Amyloid deposits are also found within several tissues in relation to diseases such as type 2 diabetes and systemic amyloidosis[9]. So far, 36 amyloid fibre proteins have been identified in humans. As disease-related structures, special attention is given to their formation mechanisms with the ultimate aim to understand their relationships with disorder development[10,11]. It is indeed of paramount importance to decipher the key steps at the origin of their formation and accumulation into amyloid deposits, and to characterize the toxic species and their generation[11]. Another equally important research axis concerns the detection of amyloid deposits for the in vivo diagnosis of amyloidosis. Indeed, in the case of Alzheimer's and Parkinson's diseases, for instance, a diagnosis is needed not only for better medical care but also for the development of new therapies[12,13]. Currently, the diagnosis is based on the detection of mild cognitive impairment, which is not without ambiguity. As a consequence, biomarkers are sought to complete the diagnosis and targeting the amyloid deposits seems to be promising for that purpose.

Here, we describe intrinsic ultraviolet–visible–near-infrared (UV–vis–NIR) optical properties of amyloid fibres, drawn from the characterization of amyloid fibres made of 13 proteins either involved in diseases or not (Table 1). Besides the blue luminescence that has been already described in vitro for amyloid fibres, other protein aggregates and within metabolite amyloid-like structures[14–21], we report a NIR signal specific to the amyloid fibre structure. Although the underlying basic phenomena remain mostly unknown so far, these optical properties are of considerable interest for the investigation (both in vitro and in vivo) of amyloid-based disease development. The two types of optical signal not only allow label-free kinetic studies of the fibre self-assembly mechanisms but also the monitoring of the different key steps. The blue luminescence allows amyloid deposits to be characterized within biological samples (mice and human) and their morphology to be assessed within the biological environment without the need for specific staining procedures. Ultimately, the NIR signal is of interest. We demonstrate that it allows for the detection of amyloid deposits within the brain of living rodents using in vivo, non-invasive, real-time and contrast-agent-free imaging through the skull of mice. Its significance for application in human amyloidosis needs to be further researched.

UV–vis–NIR properties of amyloid fibres

The luminescent properties of amyloid fibres spanning from the visible to the NIR are shown in vitro with the Het-s prion domain forming an amyloid fibre suspension (Fig. 1a) and by fluorescence microscopy of highly oriented amyloid fibres within a microwire (Fig. 1b), resulting from the self-organization of a drop drying between two tips (Supplementary Fig. 1). Depending on the excitation wavelength, the microwire appears with colours ranging from blue (with an excitation in the near-UV) to the red-NIR (Fig. 1b). These observations performed on dry aligned fibres can be related to spectroscopic measurements on a suspension of amyloid fibres

Table 1 | Change of luminescence properties of 13 amyloid proteins before and after fibre formation

Polypeptide	Trp/Tyr/Phe	Extinction coefficient (M^{-1} cm^{-1})[b]	Blue luminescence enhancement	NIR Stokes shift (nm) (exc., 640 nm)
Disease related				
$A\beta_{1-42}$	0/1/3		×3	56
htau	0/1/1		×6	53
α-Synuclein	0/4/2		×3.5	58
TTR (V30M)	2/5/4		×3	55
IAPP	0/1/2		×3	55
Model proteins				
Het-s prion domain	1/1/1		×8	60
β-Lactoglobulin	2/4/3	~450 (340 nm)	×3.5	62
α-Lactalbumin	4/4/4		×1	52
HSA	3/21/30		×1	56
Lysozyme	6/3/3	~300 (360 nm)	×4	63
Insulin	0/4/3		×36	56
Peptides				
CSNNFGA[a]	0/0/1	~400 (330 nm)		55
NNLAIVTA[a]	0/0/0			58

[a]The enhancement of the peptides CSNNFGA and NNLAITVA is unknown, due to the lack of lag phase and fast aggregation into fibres. (See Methods for details on the formation of the various amyloid fibres.) [b]The numbers in brackets represent the respective maximum of the excitation band (at which the extinction coefficients are estimated) that differs for the model proteins β-lactoglobulin and lysozyme, and the peptide CSNNFGA. Trp, Tyr and Phe are the amino acids tryptophan, tyrosine and phenylalanine, respectively. HSA, human serum albumin.

made of the Het-s prion domain (Fig. 1a). On near-UV excitation, blue luminescence is first detected. The emission peak is quite broad and its maximum experiences a bathochromic shift with excitation of increasing wavelength. Luminescent properties can also be observed in the red-NIR range; the emission maximum depends drastically on the excitation wavelength. The intensity of the NIR signal is found to be approximately 30 times lower than the intensity of the blue luminescence; the exact ratio depending on the protein concentration.

Similar observations can be made with amyloid fibres made of $A\beta_{1-42}$, both in vitro and within a biological context (Fig. 1c,d). In vitro, the optical properties of an $A\beta_{1-42}$ amyloid fibre suspension (Fig. 1c) are similar to those described above. In vivo, $A\beta_{1-42}$ forms amyloid deposits within the brain of aged mice with Alzheimer's disease (18 months)[22,23], overexpressing human $A\beta_{1-42}$, that can be detected ex vivo within the cortex area on labelling with thioflavin S (Supplementary Fig. 2). These amyloid deposits can be detected without staining by fluorescence microscopy (Fig. 1d) using the same parameters mentioned above for the aligned amyloid fibres. Importantly, nothing noticeable can be seen in transmission. These stains are not seen on brain sections of middle-age control mice (Supplementary Fig. 3). Two different patterns can be distinguished: sharp spots and much broader stains with a denser centre and a more diffuse periphery (Fig. 1d). Only the last pattern is typical of amyloid deposits[22,23]. The sharper spots are barely detectable in the blue range (Fig. 1d), suggesting that they are not indicative of amyloid deposits. We tentatively linked them to lipofuscins, granules of lipids and pigments with a strong auto-fluorescence[20,24,25],

that are known to accumulate with age within several organs[26,27], as observed in the control aged mouse brain (Supplementary Fig. 4), showing that their presence is not univocally related to Alzheimer's disease[28,29].

Blue luminescence in vitro and from human samples
In agreement with previous studies[14–17], blue luminescence is observed for all amyloid fibres investigated here (Table 1). This luminescent behaviour is illustrated for representative proteins (Fig. 2 and Supplementary Fig. 5) as well as for proteins involved in diseases (Fig. 1c and Supplementary Fig. 6). Although the luminescent behaviour is not identical for every amyloid fibre (Table 1), generic characteristics can be determined (see Supplementary Information). The emission maxima are invariably located within the 430–450 nm spectral range and are dependent on the excitation wavelength for most fibres. A weak blue luminescence is usually detected for the monomeric polypeptides (Fig. 2 and Supplementary Fig. 5). However, a notable enhancement of the intensity is observed on fibre formation (Table 1). The excitation spectra are remarkably similar with a band centred at approximately 350–370 nm (Fig. 2a and Supplementary Fig. 5). When possible, estimations of the molar extinction (ε) for this transition give values of approximately 300–450 M^{-1} cm^{-1} (Table 1 and Supplementary Fig. 5). The luminescence quantum yield is rather low[30] (approximately 0.01) with typical lifetimes of approximately 1–3 ns (refs. [14,16,17]). Several tentative explanations have been proposed for this luminescence, such as the occurrence of quantum confinement due to the sub-10 nm size of the supramolecular assemblies[18,31] or charge delocalization within the H-bond network stabilizing the fibres[32]. A similar blue luminescence, termed 'non-traditional intrinsic luminescence'[33], has been reported for supramolecular architectures lacking traditional luminophores, including amyloid fibres. This luminescence is related to the aggregation/confinement of electron-rich heteroatomic moieties[33].

Strikingly, the blue luminescence we observed is intense enough to allow the monitoring of the structure of amyloid deposits by confocal microscopy within a human brain section from a patient with Alzheimer's disease. Figure 3 shows 3D reconstructions of two amyloid deposits with different structures; typical sections are shown in the insets. The first (Fig. 3a) is a dense packing with fibrillary structures that can be distinguished on the periphery only, whereas the second (Fig. 3b) is a fibre embedded with a more homogenous distribution of fibres. Their surroundings can also be visualized. The first structure is surrounded by brain tissue and looks like a 'pompom' associated with a blood vessel (Fig. 3a); very similar to deposits observed in brain tissue taken from human patients[34] or mice[35] with Alzheimer's disease. The second deposit seems more isolated (Fig. 3b). Videos showing the internal structures (Supplementary Videos 1 and 2) and the 3D external envelopes (Supplementary Videos 3 and 4) of both amyloid deposits have been built from the sequential confocal images.

In vitro NIR signal
The NIR signal is unequivocally linked to the supramolecular structure of the amyloid fibres (Supplementary Fig. 1) since no signal is recorded in the case of monomeric proteins (Fig. 2 and Supplementary Fig. 5). Within the wavelength range investigated here, the maximum of the NIR signal continuously shifts with a linear dependency between the excitation and the maximum emission wavelengths (Supplementary Fig. 7), indicating a constant Stokes shift of approximately 55–60 nm (Table 1). The origins of this luminescence, which is also present within amyloid fibres without aromatic side-chains (Supplementary Fig. 5), remain to be understood. This NIR signal has the following two remarkable features: (1) it is detectable within a very broad wavelength range with a constant Stokes shift and (2) it has a rather narrow emission,
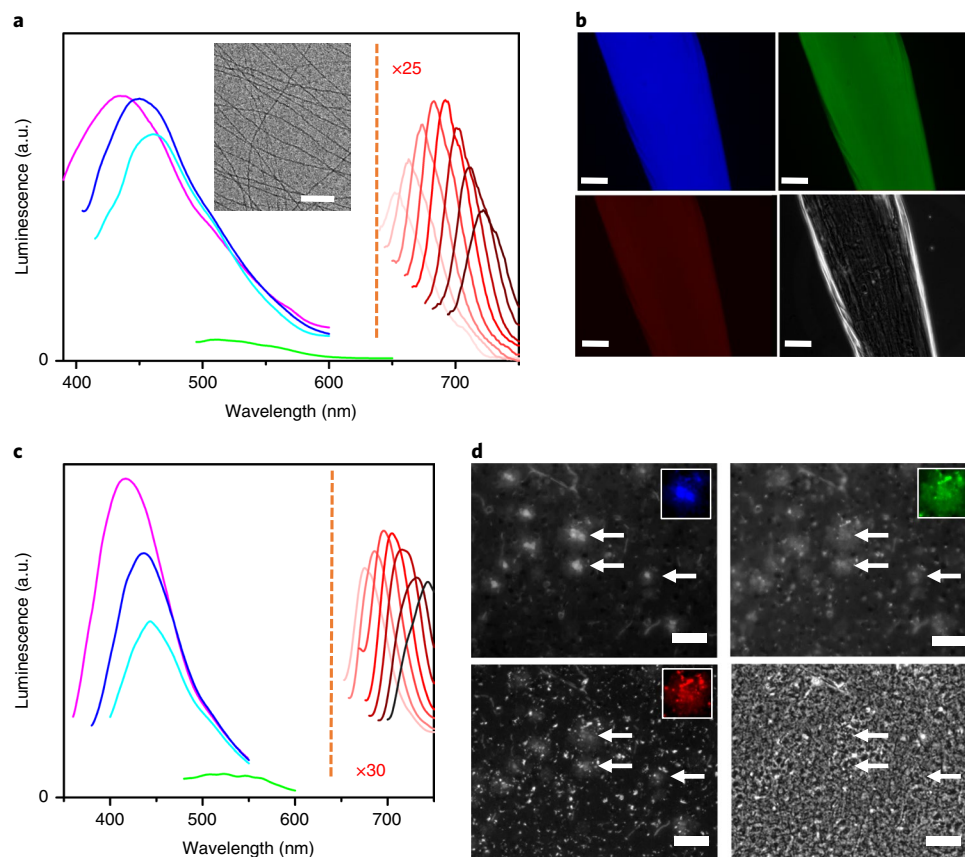
Fig. 1 | UV–vis–NIR luminescence of Het-s prion domain and Aβ$_{1-42}$ amyloid fibres. a,c, Luminescence of dispersions of Het-s prion domain (**a**) and Aβ$_{1-42}$ (**c**) amyloid fibres in buffer. Excitation wavelengths: 340 nm (pink), 360 nm (blue), 380 nm (cyan) and 440 nm (green), and from 600 to 670 nm (red colour scale). A multiplying factor (either ×25 or ×30) has been applied to the NIR spectra to show both types of luminescence in the same graph. Inset in **a**: TEM image of Het-s prion domain. Scale bar, 100 nm. **b,d**, Fluorescence microscopy. Transmission mode (bottom right) and fluorescence microscopy images with emission in the UV–vis ($\lambda_{exc}=390\pm10$ nm, $\lambda_{em}=460\pm50$ nm) (top left), green ($\lambda_{exc}=475\pm10$ nm, $\lambda_{em}=530\pm50$ nm) (top right) and NIR ($\lambda_{exc}=620\pm60$ nm, $\lambda_{em}=700\pm75$ nm, false red colour) (bottom left). **b**, Aligned Het-s prion domain amyloid fibres. Scale bars, 100 μm. **d**, Sections of the cortex area of mice with Alzheimer's disease. Scale bars, 50 μm. Amyloid deposits are visible without extrinsic fluorophores (arrows).
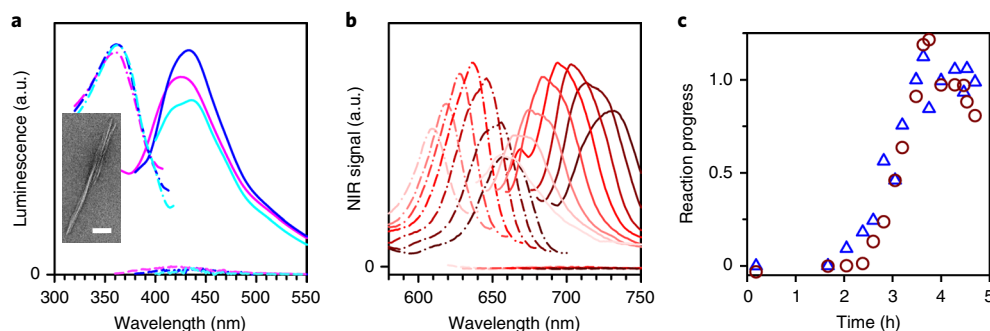

Fig. 2 | Luminescence properties of insulin amyloid protein during fibre growth process. a, Blue luminescence of insulin amyloid fibres. Emission spectra of fibres (continuous lines), λ_{exc}: 340 nm (pink), 360 nm (blue) and 380 nm (cyan), and of monomers (dashed lines, same colours); excitation spectra of insulin amyloid fibres (dash-dot lines), λ_{em}: 430 nm (pink), 444 nm (blue) and 458 nm (cyan). Inset: TEM image of insulin amyloid fibres. Scale bar, 100 nm. **b**, NIR luminescence of insulin amyloid fibres. Emission spectra of fibres (continuous lines, different red shades), λ_{exc}: from 600–670 nm, and of monomers (dashed lines, same colours); excitation spectra of insulin amyloid fibres (dash-dot lines: the emission wavelengths correspond to the maximum emission wavelength). **c**, Kinetics of formation of amyloid fibres of insulin simultaneously monitored through blue luminescence (blue triangles: λ_{exc}, 360 nm) and the NIR signal (dark red circles: λ_{exc}, 640 nm).

narrowing further as the width of the emission monochromator slit width decreases (Supplementary Fig. 8), suggesting that the NIR signal is due to an inelastic light scattering rather than from a relaxation of excited states within the fibres. This tentative explanation

is further supported by the impossibility of determining lifetimes for the NIR signal (value lower than 0.1 ns), whereas expected values of lifetimes for singlet and triplet excited states (approximately 1 ns versus approximately 100 μs) could be measured for
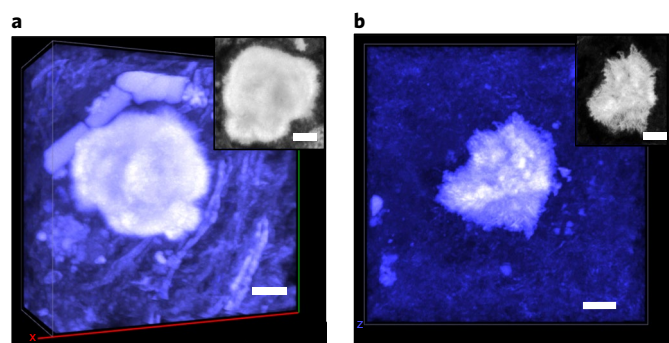
Fig. 3 | Ex vivo confocal microscopy images of amyloid deposits in brain slices from pateints with Alzheimer's disease within the hippocampus area. a,b, 3D modelling of the two amyloid deposits from 60 sections recorded through blue emission (λ_{exc}, 350–420 nm; λ_{em}, 440–500 nm) images. The 3D modelling images were analysed with the Vaa3D software. Insets: typical sections of the reconstructed amyloid deposits monitored in the blue range. Scale bars, 5 μm.

lysozyme amyloid fibres (not shown). In addition, the Stokes shift is around 1,200–1,400 cm^{-1} (Supplementary Fig. 8), in good agreement with the Raman shift of the amide I–III bands of proteins[36]. Moreover, the appearance of the NIR signal seems to be correlated with an enhancement of the Raman signal due to the organization of the proteins within the amyloid fibres[37] (Supplementary Fig. 9). Similarly to the blue photoluminescence, the NIR signal intensity increases steadily with the protein concentration without aggregation-induced quenching (Supplementary Fig. 10). Altogether, these observations point towards an enhancement of the Raman signal, due to protein self-assembly into highly organized amyloid fibres[37] as an explanation for the NIR signal. To date, only a preliminary correspondence between the position of the NIR signal and the Raman spectrum (several bands between 1,000 cm^{-1} and 1,700 cm^{-1}) has been observed. Unexpectedly for a Raman spectrum, the position of the NIR signal shifts with the excitation wavelength: from 1,400 cm^{-1} to 1,160 cm^{-1} within the wavelength range investigated (Supplementary Fig. 8). This effect might be due to the fact that (1) these experiments were performed with a spectrofluorometer where the excitation is not monochromatic but has a finite bandwidth (slits), in contrast to a Raman spectrometer that uses monochromatic laser light, and (2) the NIR signal excitation seems to have a maximum (Fig. 2). When the excitation wavelength increases and moves away from its optimal value (as is the case in Supplementary Fig. 8), the contribution of high-energy photons to the emitted light will increase compared with that of lower-energy photons. This will result in an apparent decrease of the energy difference between the excitation spectrum and the emission spectra, that is, an apparent decrease of the Stokes shift as the excitation wavelength increases. Nonetheless, the correspondence between our NIR signal and Raman scattering is not unambiguously established; other possibilities such as optical effects due to the size (hundreds of nanometres) and shape (high aspect ratio) of amyloid fibres remains to be evaluated.

Kinetics of fibril formation without external probe

The investigation of amyloid fibre formation is of prime importance to unravel the molecular events at the origin of disease development. To date, a fluorescent marker must be used to monitor fibre formation, the most commonly used being thioflavin T (ThT)[10,11]. However, several assumptions lie behind its use[38] concerning (1) ThT effect on the amyloid fibril formation kinetics and (2) the proportionality between the ThT signal and the amount of amyloid fibres. The blue luminescence and NIR signal should be valuable
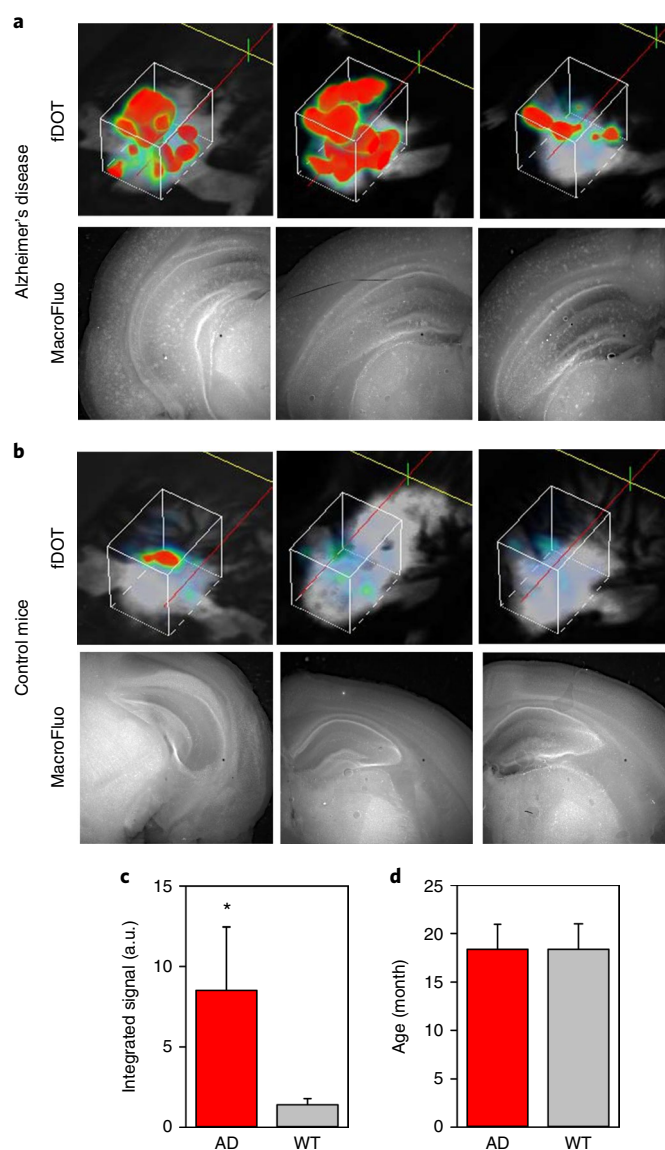

Fig. 4 | Detection of amyloid deposits by 3D NIR imaging in mice with Alzheimer's disease and control mice. a,b, Top: fDOT imaging on live animals (λ_{exc}, 690 nm (laser light) and λ_{em}, 730 ± 30 nm). Bottom: fresh brain sections from the cortex area were observed with the MacroFluo set-up with a 515–560 nm excitation and a 590-nm long-pass emission filter. **c**, Higher NIR signal intensities were observed in the brain volume of mice with Alzheimer's disease (AD) compared with control (wild-type, WT) mice as measured in the 11 mice per group. **d**, Age distribution of both populations. The error bars correspond to the standard errors of the mean. *$P = 0.044$.

intrinsic probes of fibre formation. The possibility of using blue luminescence has already been demonstrated[17]. However, it remains ambiguous due to the fact that blue luminescence has been reported for other protein aggregates than amyloid fibres, such as crystals for instance[19,33]. The NIR signal, which is observed only on the formation of amyloid fibres, holds potential for becoming a truly unambiguous probe. The NIR signal and blue luminescence are proportional to the protein concentration (Supplementary Fig. 11); when Aβ$_{1-42}$ fibres are depolymerized by adding 1,1,1,3,3,3-hexafluoropropan-2-ol (HFIP), the NIR signal vanishes (Supplementary Fig. 11). As a proof-of-concept demonstration, the amyloid fibre formation of insulin has been simultaneously monitored by blue
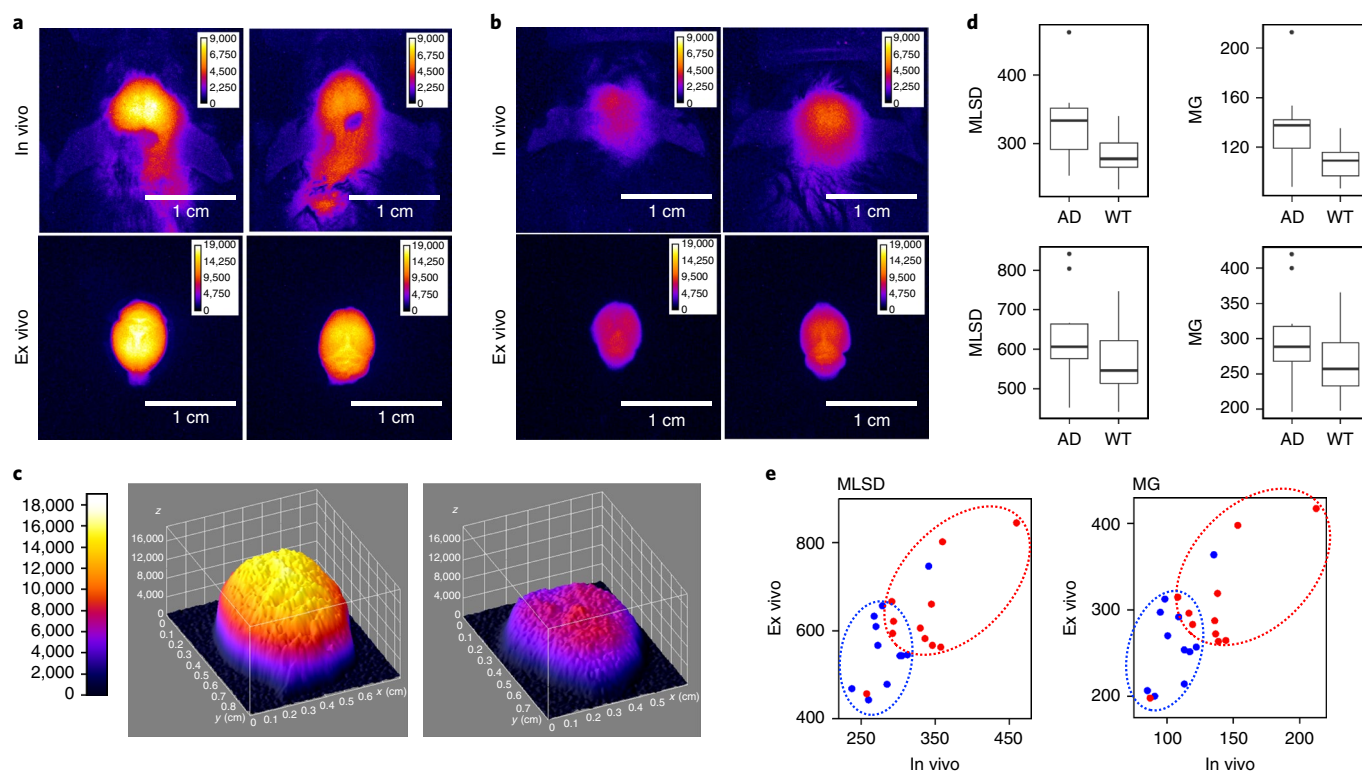
Fig. 5 | Non-invasive detection of amyloid deposits by 2D NIR imaging using Fluobeam800. a,b, In vivo 2D imaging of anaesthetized mice was performed by scanning the head of the animals (top panels) and ex vivo on the corresponding brains after they were removed (bottom panels). Two representative mice from the group with Alzheimer's disease (**a**) and control group (**b**) are presented. **c**, Mapping of the NIR signal intensity distribution within a 3D graph. Representative examples of the NIR fluorescence of the brain region of a mouse with Alzheimer's disease (left) and of a control mouse (right) are presented. Colour scale bars in **a**–**c** indicate fluorescence intensity in arbitrary units. **d**, Box plots of the MLSD and MG values calculated (see Methods) for each animal (AD, $n = 11$ and WT, $n = 11$) in vivo (top) and ex vivo (bottom). The bold lines correspond to the median values. The box and bar sizes were calculated based on Tukey's rules. The dots correspond to outliers. **e**, Ex vivo values of MLSD and MG versus in vivo values of mice with Alzheimer's disease (red circles) and control mice (blue circles).

luminescence and NIR signal changes (Fig. 2c). Obviously, the blue luminescence signal begins to appear before the NIR signal as seen after 2 h (Fig. 2c and Supplementary Fig. 12). This suggests that the phenomenon at the origin of the blue luminescence precedes the fibre growth, likely because of early intermediates. In a separate experiment, we checked that the NIR signal superimposes with the ThT fluorescence build up (Supplementary Fig. 13).

Imaging of amyloid deposits using in vivo NIR signals

The intrinsic NIR signal of amyloid fibres is of particular interest as it falls within the so-called 'diagnostic windows'. NIR photons are attractive for non-invasive analyses as they can penetrate deep into biological tissues, opening the door towards non-invasive imaging for monitoring biological functions/dysfunctions within living tissues longitudinally over time[39,40]. Owing to its particular nature, it was impossible to measure a quantum yield for the NIR signal. To estimate its intensity, we compared it with that of cyanine 5.5, a fluorophore used for in vivo NIR imaging and of known quantum yield[41] (Supplementary Fig. 14). After normalization of the concentrations, the NIR signal of amyloid fibres seemed to be around three orders of magnitude weaker than that of cyanine 5.5. However, this low signal could be compensated in vivo due to the high density of amyloid deposits. Indeed, the in vitro NIR signal increases steadily with the protein concentration, that is, without aggregation-induced quenching (Supplementary Fig. 10), and the signal intensity of a dried droplet is high (Supplementary Fig. 14).

The use of continuous-wave NIR fluorescence-enhanced diffuse optical tomography (fDOT) allows for a fast, 3D and quantitative measurement of the NIR signal distribution in the scanned volume of interest at each time point. Disease progression can thus be precisely and accurately monitored in a given animal over time[42,43]. fDOT imaging ($\lambda_{exc} = 690$ nm and $\lambda_{em} = 730 \pm 30$ nm) was performed on 11 advanced-age mice with Alzheimer's disease and on 11 control wild-type mice (Fig. 4). Live animal imaging was performed non-invasively and without the use of any contrast agent. Both populations had similar age distributions (18.4 ± 2.6 months for both groups) (Fig. 4d). Figure 4a,b (top panels) show typical 3D brain images (total integrated signal) of mice with Alzheimer's disease and control mice. Overall, the NIR signal was 6 times more intense in mice with Alzheimer's disease (Fig. 4c) compared with that in the controls ($p < 0.05$, Student t-test). Fresh brain sections from these same mice were then observed by epifluorescence in the visible wavelength range using a MacroFluo fluorescence stereomicroscope. Typical granular structures could be observed within the cortex area of mice with Alzheimer's disease whereas the cortex area of control mice appeared completely devoid of particular patterns (Fig. 4a,b, bottom panels), indicating that the fDOT intensity increase was related to the accumulation of amyloid deposits. The excitation wavelength used for these fDOT experiments, 690 nm, together with that of the subsequent 2D NIR imaging, 780 nm, were far beyond the maximum of lipofuscin's emission spectrum, 600–650 nm (refs. [20,30]). Therefore, it is very unlikely that the NIR signal increase was due to lipofuscin. This illustrates an advantage of the amyloid NIR signal. It occurs in an extremely broad wavelength range (Supplementary Fig. 8) and, importantly, enables amyloid fibres to be distinguished from other possible sources of luminescence.

The increased in vivo NIR signal measured using fDOT could also be seen using non-invasive 2D NIR imaging (Fluobeam800)[44] performed on the head of living mice under anaesthesia (Fig. 5a,b, top panels) as well as on extracted whole brains after the mice were killed (Fig. 5a,b, bottom panels). We then hypothesized that the NIR-signal-contrasted granular structures seen on the MacroFluo images (Fig. 4) should also be registered by Fluobeam800, although the presence of heterogeneities was not distinguishable by the naked eye in these images. This indeed occurred by mapping the NIR signal intensity distribution in the image in a 3D graph (Fig. 5c). By these means, mice with Alzheimer's disease were shown to display both higher NIR signal intensities and increased speckles compared with the control group. The variation of intensity of each pixel was compared to its closest neighbours (mean local standard deviation, MLSD), or as a function of the slopes of variations (mean gradient, MG), on brain regions-of-interest (see Methods). These methods of analysis allowed us to demonstrate that we could detect speckles due to pixel-to-pixel heterogeneities more often in mice with Alzheimer's disease than in the wild-type group, both in images taken non-invasively in living animals (Fig. 5d, top panels) and in images taken ex vivo of whole brains removed after the mice were killed (Fig. 5d, bottom panels). Thus, by using MLSD and MG, two populations stood out and mice with Alzheimer's disease could be distinguished from the control mice (Fig. 5e) with only two exceptions (one in each panel, either 'AD' or 'control'). In particular, one mouse with Alzheimer's disease displayed several dark skin marks that definitely interfered in the NIR signal evaluation and led to misattribution.

Conclusions

In summary, we describe two optical signatures of amyloid fibres: a luminescence in the blue and a NIR signal, which can be observed in vitro and in vivo from tissues. These features allow for the direct detection of amyloid structures without labelling. In vitro, this is of particular interest to monitor the fibrillation kinetics without the need of an extrinsic probe that can possibly interfere with the reaction. Moreover, it seems that the two types of signature reflect different phenomena involved in the self-assembly mechanism. Furthermore, such detection and quantification could allow also investigations on ex vivo thick tissue sections without staining procedures. The NIR signal is of particular interest for the in vivo detection of amyloid deposits that should be further investigated in the human brain[39] and also in other organs where amyloidosis is involved. This could establish this amyloid-specific NIR signal as a new blueprint for the study of amyloidosis. We indeed show that the aged mouse model of Alzheimer's disease has a strong and heterogeneous NIR signal that can be detected by 3D imaging in the NIR but also by using non-invasive and real-time 2D NIR imaging on live animals. In case the NIR signal would correspond to an enhancement of spontaneous Raman scattering, this would be of high interest not only for detecting but also for characterizing in situ amyloid deposits, in particular via stimulated Raman scattering approaches[45,46]. Moreover, as amyloid fibres attract considerable interest for the design of functional bionanomaterials, taking advantage of their peculiar optical properties described here can be envisioned[47–49]. This would extend the scope of the results presented here beyond neurodegenerative diseases, opening the door to bio-inspired photonic devices exploiting the so far vastly unexplored visible-to-NIR luminescent properties of proteins self-assembled into amyloid fibres.

Online content

Any methods, additional references, Nature Research reporting summaries, source data, statements of code and data availability and associated accession codes are available at https://doi.org/10.1038/s41566-019-0422-6.

References

1. Eisenberg, D. & Jucker, M. The amyloid state of proteins in human diseases. *Cell* **148**, 1188–1203 (2012).
2. Knowles, T. P. J., Vendruscolo, M. & Dobson, C. M. The amyloid state and its association with protein misfolding diseases. *Nat. Rev. Mol. Cell Biol.* **15**, 384–396 (2014).
3. Doussineau, T. et al. Mass determination of entire amyloid fibrils by using mass spectrometry. *Angew. Chem. Int. Ed.* **55**, 2340–2344 (2016).
4. Knowles, T. P. J. & Mezzenga, R. Amyloid fibrils as building blocks for natural and artificial functional materials. *Adv. Mater.* **28**, 6546–6561 (2016).
5. Aumüller, T. & Fändrich, M. Protein chemistry: catalytic amyloid fibrils. *Nat. Chem.* **6**, 273–274 (2014).
6. Altamura, L. et al. A synthetic redox biofilm made from metalloprotein–prion domain chimera nanowires. *Nat. Chem.* **9**, 157–163 (2017).
7. Kovacs, G. G. Molecular pathological classification of neurodegenerative diseases: turning towards precision medicine. *Int. J. Mol. Sci.* **17**, 189 (2016).
8. Jucker, M. & Walker, L. C. Self-propagation of pathogenic protein aggregates in neurodegenerative diseases. *Nature* **501**, 45–51 (2013).
9. Sipe, J. D. et al. Amyloid fibril proteins and amyloidosis: chemical identification and clinical classification International Society of Amyloidosis 2016 Nomenclature Guidelines. *Amyloid* **23**, 209–213 (2016).
10. Knowles, T. P. J. et al. An analytical solution to the kinetics of breakable filament assembly. *Science* **326**, 1533–1537 (2009).
11. Glabe, C. G. Common mechanisms of amyloid oligomer pathogenesis in degenerative disease. *Neurobiol. Aging* **27**, 570–575 (2006).
12. Cummings, J. L., Doody, R. & Clark, C. Disease-modifying therapies for Alzheimer disease: challenges to early intervention. *Neurology* **69**, 1622–1634 (2007).
13. Stower, H. Searching for Alzheimer's disease therapies. *Nat. Med.* **24**, 894–897 (2018).
14. Mercato, L. L. del et al. Charge transport and intrinsic fluorescence in amyloid-like fibrils. *Proc. Natl Acad. Sci. USA* **104**, 18019–18024 (2007).
15. Tcherkasskaya, O. Photo-activity induced by amyloidogenesis. *Protein Sci.* **16**, 561–571 (2007).
16. Chan, F. T. S. et al. Protein amyloids develop an intrinsic fluorescence signature during aggregation. *Analyst* **138**, 2156–2162 (2013).
17. Pinotsi, D., Buell, A. K., Dobson, C. M., Schierle, G. S. K. & Kaminski, C. F. A label-free, quantitative assay of amyloid fibril growth based on intrinsic fluorescence. *ChemBioChem* **14**, 846–850 (2013).
18. Handelman, A., Beker, P., Amdursky, N. & Rosenman, G. Physics and engineering of peptide supramolecular nanostructures. *Phys. Chem. Chem. Phys.* **14**, 6391–6408 (2012).
19. Shukla, A. et al. A novel UV laser-induced visible blue radiation from protein crystals and aggregates: scattering artifacts or fluorescence transitions of peptide electrons delocalized through hydrogen bonding? *Arch. Biochem. Biophys.* **428**, 144–153 (2004).
20. Zipfel, W. R. et al. Live tissue intrinsic emission microscopy using multiphoton-excited native fluorescence and second harmonic generation. *Proc. Natl Acad. Sci. USA* **100**, 7075–7080 (2003).
21. Shaham-Niv, S. et al. Intrinsic fluorescence of metabolite amyloids allows label-free monitoring of their formation and dynamics in live cells. *Angew. Chem. Int. Ed.* **57**, 12444–12447 (2018).
22. Kuo, Y.-M. et al. Comparative analysis of amyloid-β chemical structure and amyloid plaque morphology of transgenic mouse and Alzheimer's disease brains. *J. Biol. Chem.* **276**, 12991–12998 (2001).
23. Matsuoka, Y. et al. Inflammatory responses to amyloidosis in a transgenic mouse model of Alzheimer's disease. *Am. J. Pathol.* **158**, 1345–1354 (2001).
24. Marmorstein, A. D., Marmorstein, L. Y., Sakaguchi, H. & Hollyfield, J. G. Spectral profiling of autofluorescence associated with lipofuscin, Bruch's Membrane, and sub-RPE deposits in normal and AMD eyes. *Invest. Ophthalmol. Vis. Sci.* **43**, 2435–2441 (2002).
25. Haralampus-Grynaviski, N. M. et al. Spectroscopic and morphological studies of human retinal lipofuscin granules. *Proc. Natl Acad. Sci. USA* **100**, 3179–3184 (2003).
26. Youssef, S. A. et al. Pathology of the aging brain in domestic and laboratory animals, and animal models of human neurodegenerative diseases. *Vet. Pathol.* **53**, 327–348 (2016).
27. Gilissen, E. P. et al. A neuronal aging pattern unique to humans and common chimpanzees. *Brain Struct. Funct.* **221**, 647–664 (2016).
28. Dowson, J. H., Mountjoy, C. Q., Cairns, M. R., Wilton-Cox, H. & Bondareff, W. Lipopigment changes in Purkinje cells in Alzheimer's disease. *J. Alzheimer's Dis.* **1**, 71–79 (1998).
29. D'Andrea, M. R. et al. Lipofuscin and Aβ42 exhibit distinct distribution patterns in normal and Alzheimer's disease brains. *Neurosci. Lett.* **323**, 45–49 (2002).

30. Niyangoda, C., Miti, T., Breydo, L., Uversky, V. & Muschol, M. Carbonyl-based blue autofluorescence of proteins and amino acids. *PLoS ONE* **12**, e0176983 (2017).
31. Tao, K. et al. Quantum confined peptide assemblies with tunable visible to near-infrared spectral range. *Nat. Commun.* **9**, 3217 (2018).
32. Pinotsi, D. et al. Proton transfer and structure-specific fluorescence in hydrogen bond-rich protein structures. *J. Am. Chem. Soc.* **138**, 3046–3057 (2016).
33. Tomalia, D. A. et al. Non-traditional intrinsic luminescence: inexplicable blue fluorescence observed for dendrimers, macromolecules and small molecular structures lacking traditional/conventional luminophores. *Prog. Polym. Sci.* **90**, 35–117 (2019).
34. Plascencia-Villa, G. et al. High-resolution analytical imaging and electron holography of magnetite particles in amyloid cores of Alzheimer's disease. *Sci. Rep.* **6**, 24873 (2016).
35. Meyer, E. P., Ulmann-Schuler, A., Staufenbiel, M. & Krucker, T. Altered morphology and 3D architecture of brain vasculature in a mouse model for Alzheimer's disease. *Proc. Natl Acad. Sci. USA* **105**, 3587–3592 (2008).
36. Michael, R. et al. Hyperspectral Raman imaging of neuritic plaques and neurofibrillary tangles in brain tissue from Alzheimer's disease patients. *Sci. Rep.* **7**, 15603 (2017).
37. Flynn, J. D., Jiang, Z. & Lee, J. C. Segmental ^{13}C-labeling and Raman microspectroscopy of α-synuclein amyloid formation. *Angew. Chem. Int. Ed.* **130**, 17315–17318 (2018).
38. Xue, C., Lin, T. Y., Chang, D. & Guo, Z. Thioflavin T as an amyloid dye: fibril quantification, optimal concentration and effect on aggregation. *R. Soc. Open Sci.* **4**, 160696 (2017).
39. Hong, G. et al. Through-skull fluorescence imaging of the brain in a new near-infrared window. *Nat. Photon.* **8**, 723–730 (2014).
40. Hilderbrand, S. A. & Weissleder, R. Near-infrared fluorescence: application to in vivo molecular imaging. *Curr. Opin. Chem. Biol.* **14**, 71–79 (2010).
41. Bouteiller, C. et al. Novel water-soluble near-infrared cyanine dyes: synthesis, spectral properties, and use in the preparation of internally quenched fluorescent probes. *Bioconj. Chem.* **18**, 1303–1317 (2007).
42. Koeing, A. et al. In vivo mice lung tumor follow-up with fluorescence diffuse optical tomography. *J. Biomed. Opt.* **13**, 011008 (2008).
43. Koenig, A. et al. Fluorescence diffuse optical tomography for free-space and multifluorophore studies. *J. Biomed. Opt.* **15**, 016016 (2010).
44. Josserand, V. et al. Electrochemotherapy guided by intraoperative fluorescence imaging for the treatment of inoperable peritoneal micro-metastases. *J. Control. Rel.* **233**, 81–87 (2016).
45. Saar, B. G. et al. Video-rate molecular imaging in vivo with stimulated Raman scattering. *Science* **330**, 1368–1370 (2010).
46. Camp, C. H. Jr et al. High-speed coherent Raman fingerprint imaging of biological tissues. *Nat. Photon.* **8**, 627–634 (2014).
47. Hanczyc, P., Samoc, M. & Norden, B. Multiphoton absorption in amyloid protein fibres. *Nat. Photon.* **7**, 969–972 (2013).
48. Tao, K., Makam, P., Aizen, R. & Gazit, E. Self-assembling peptide semiconductors. *Science* **358**, eaam9756 (2017).
49. Berger, O. et al. Light-emitting self-assembled peptide nucleic acids exhibit both stacking interactions and Watson–Crick base pairing. *Nat. Nanotechnol.* **10**, 353–360 (2015).

Author contributions

J.P. and V.F. conceived and designed the work, and wrote most of the paper. J.P., S-J.L., D.I., O.C.-P. and C.V. performed the in vitro characterizations of the amyloid fibres. A.R., T.D. and P.R. conceived, performed and analysed the X-ray scattering experiments. M.M.S. and E.K. collected and prepared the human samples. J.P. and C.M. designed and performed the ex vivo experiments. V.J., M.G., J.V., A.F., Y.U. and J.L.C. performed the 3D and 2D fluorescence imaging and analysed the data. J.P., C.M. and V.F. coordinated all experiments and compiled the results. J.P., C.M., P.R. and V.F. edited the text. All co-authors discussed and commented on the manuscript.

Competing interests

The authors declare no competing interests.

Additional information

Supplementary information is available for this paper at https://doi.org/10.1038/s41566-019-0422-6.

Reprints and permissions information is available at www.nature.com/reprints.

Correspondence and requests for materials should be addressed to V.F.

Publisher's note: Springer Nature remains neutral with regard to jurisdictional claims in published maps and institutional affiliations.

Methods

Fibril growth. The amyloid fibres of the Het-s prion domain were obtained as previously described[3]. The $A\beta_{1-42}$, IAPP and TTR(V30M) fibres were formed as previously described[50]. The CSNNFGA peptide (Genecust) is a derived sequence from IAPP, so CSNNFGA fibres were formed following the same protocol as for IAPP fibres. The hTau and α-synuclein fibres were formed as previously described[51]. Lyophilized lysozyme (Sigma-Aldrich, L-6876) and human serum albumin (Sigma-Aldrich, A-3732) were directly dissolved in a 50 mM glycine, 88 mM NaCl buffer and adjusted to pH 2.7 to obtain, respectively, a final concentration of 1 mM and 250 μM, incubated at 65 °C over 3 days. For lysozyme fibrillation, a rotating shaker (500 r.p.m.) was used[52]. Insulin fibres were formed using lyophilized insulin (Sigma-Aldrich, I6634-1G) in a 20% acetic acid buffer, adjusted to pH 1.7 at 40 °C on a rotating shaker (500 r.p.m.) over 10 h. Lyophilized β-lactoglobulin (Sigma-Aldrich, L3908-5G) was dissolved in deionized water (2 mM), adjusted to pH 2 and 335 K, filtered through a 0.22 μm filter before 10 days of incubation, adapted from published protocols[53]. The α-lactalbumin (Sigma-Aldrich, L6010-1G) fibres were obtained as previously described[3]. The NNLAIVTA (Proteogenix) fibres were formed in a HEPES 10 mM buffer at a final concentration of 1.5 mM at pH 7.4 (ref. [54]). All fibre morphologies were confirmed using transmission electron microscopy (TEM) analysis (performed on a Tecnai 12 microscope).

Fluorescence spectroscopy. Measurements on amyloid proteins were carried out using JASCO FP-8500 and Fluorolog FL3-22 spectrophotometers from Horiba-Jobin Yvon-Spex (equipped with a double grating excitation monochromator and an iHR320 imaging spectrometer). Each spectrum was recorded in a 1 cm path length quartz cell, with a response time of 1 s, an excitation bandwidth of 5 nm and an emission bandwidth of 10 nm. Excitation spectra of lysozyme, insulin and NNLAIVTA fibres were recorded at the maximum of the emission peak for each emission spectra, with the same parameters. Kinetic studies of insulin fibre formation were carried out using 200 μM of insulin either in the absence or in the presence of 30 μM ThT. For UV–vis and NIR emission spectra, excitations at 360 nm and at 640 nm were used, respectively. For the emission spectra of ThT, an excitation at 440 nm was used, and the emission intensity at 485 nm was used to record the kinetics. Absorption spectra were recorded using a JASCO J-815 CD-spectrophotometer, using a 1 cm path length quartz cell, with a response time of 1 s, a bandwidth of 4 nm, each 1 nm between 190 and 700 nm.

For lifetime measurements, excitation of the amyloid fibres was accomplished by a using (1) a nanoLED source with a laser diode head N-375L (full-width at half-maximum (FWHM) < 10 nm, pulse < 88 ps), (2) a nanoLED source with a laser diode head N-650L (FWHM < 10 nm, pulse < 70 ps) or (3) a nanoLED source with a LED head N-740 (FWHM 20 nm, pulse < 800 ps) from Horiba Scientific. The nanoLEDs were coupled to a Jobin Yvon NL-C2 pulse diode controller and a DH-HT time-correlated single-photon-counting (TCSPC) controller allowing the measurement of fluorescence lifetimes <100 ps and connected to the Fluorolog FL3-22 spectrometer from Horiba-Jobin Yvon-Spex. The output signal of the photomultiplier was fed to a PC and controlled and analysed with the Data Station (v2.7) and Decay Analysis (v6.8) software from Horiba Scientific. Lifetimes are averages of three independent determinations with a calculated chi-square <2.

Raman microspectroscopy. Raman spectra were recorded using a Jobin Yvon/Horiba LabRam spectrometer equipped with a liquid-nitrogen-cooled charge-coupled device (CCD) detector. The experiments were conducted in the micro-Raman mode at room temperature in a backscattering geometry. The 632.8 nm line from a HeNe laser was focused to a 1 μm² spot on the sample surface using a ×50 long working distance objective with an incident laser power close to 5.3 mW. Raman spectra were calibrated using a silicon reference spectrum at room temperature.

Wide-angle X-ray scattering. Aligned amyloid fibres made of the Het-s prion domain were obtained by drying a highly concentrated fibre suspension between two tips. The X-ray diffraction pattern was recorded at ESRF (Grenoble) on the microfocus beamline ID13 using a 2 × 2 μm² X-ray beam (energy $E = 13$ keV, wavelength $\lambda = 0.9537$ Å).

Brain sections of mice with Alzheimer's disease. Brain sections of APPswe/PSEN1dE9 mice (kindly provided by B. Larrat, Saclay, France) with Alzheimer's disease (aged 18 months) were mounted on slides without labelling. As the control, brain sections from C57/Bl6 mice were used (12 months old). Mice were deeply anaesthetized with an intraperitoneal injection of a mixture of xylazine/ketamine (3× the normal anaesthesia dose) before exsanguination under anaesthesia. Animals were intracardially perfused with phosphate buffer saline (PBS), followed by administration of a solution of paraformaldehyde (PFA; 4% in PBS) fixative solution. After the animals were killed, their brains were removed from the skull and post-fixed 24 h at 4 °C in PFA 4% and then transferred to PBS buffer with 0.1% sodium azide (NaN₃), before microtome sectioning (20 μm, Leica, VT 1000E) and being conserved mounted on a glass slide at −20 °C. All of the procedures involving animals were carried out in accordance with the European Community Council Directives. Intrinsic fluorescence properties were recorded with a Zeiss microscope Axiovert 200 M, at various wavelengths, with emission in blue ($\lambda_{exc} = 390 \pm 10$ nm, $\lambda_{em} = 460 \pm 50$ nm), green ($\lambda_{exc} = 475 \pm 10$ nm, $\lambda_{em} = 530 \pm 50$ nm),

yellow ($\lambda_{exc} = 545 \pm 25$ nm, $\lambda_{em} = 605 \pm 70$ nm) and in the NIR with false red colour ($\lambda_{exc} = 620 \pm 60$ nm, $\lambda_{em} = 700 \pm 75$ nm). Images were analysed with Carl Zeiss software and Image I 1.50 software.

Human samples. Brains were obtained by autopsies from the Department of Internal Medicine, Rehabilitation and Geriatrics, Division of Geriatrics, and the Department of Readaptation and Palliative Medicine, University Hospitals, Geneva with the approval from the Ethics Committee of the University of Geneva. We included tissues from two brain autopsies performed in 2015 on patients without (control) and with Alzheimer's disease. For neuropathological analysis, tissues blocks were taken from the hippocampus with the inferior temporal cortex (Brodmann area 20). Brain tissue was fixed in buffered formaldehyde 4% for 4 weeks. From paraffin-embedded blocks, adjacent sections 30-μm-thick were obtained and paraffin was removed using successive xylene/ethanol baths. The floating slices were conserved in phosphate-buffer saline (sodium azide 0.05%) until histological treatment. Intrinsic luminescence properties were recorded with a Zeiss confocal LSM800 microscope, at various wavelengths, in blue ($\lambda_{exc} = 350-420$ nm, $\lambda_{em} = 440-500$ nm), green ($\lambda_{exc} = 450-500$ nm, $\lambda_{em} = 480-550$ nm), and NIR ($\lambda_{exc} = 620-700$ nm, $\lambda_{em} = 640-750$ nm). Images were analysed with Carl Zeiss software, Vaa3D and Image I 1.50 software. Vaa3D is an open source, award-winning visualization and analysis software suite created mainly by Janelia Research Campus, HHMI and Allen Institute for Brain Science[55–57].

Immunohistochemistry. Frozen sections were processed for immunohistochemistry for amyloid burden staining with thioflavin S ($\lambda_{exc} = 450$ nm, $\lambda_{em} = 488$ nm) (Sigma, T1892) according to standard practice. Fluorescent images were obtained using either a Zeiss confocal LSM800 microscope or Zeiss microscope Axiovert 200 M for human and rodent tissues, respectively. Images were analysed using Carl Zeiss Zen software and Image J 1.50 f software.

In vivo and ex vivo imaging. All animal experiments were performed in accordance with the European Economic Community guidelines and the *Principles of Laboratory Animal Care* (NIH publication N 86-23 revised 1985). The protocols were approved by an animal ethics committee and received the authorization of the French Ministry of Higher Education and Research (authorization number 8854-2017031314338357).

Female APPswe/PSEN1dE9 and C57/Bl6 mice ($n = 11$ per group) were bred until they were 18.4 ± 0.7 months old. The day before imaging, mice were anaesthetized (isoflurane/air 4% for induction and 1.5% thereafter) and their heads shaved. For non-invasive, continuous-wave NIR fDOT imaging, anaesthetized mice were placed in a previously described prototype imaging system[42]. Briefly, the heads were illuminated with a monochromatic 690 nm laser light. The irradiance on the imaging field was 14 mW cm⁻². The re-emitted signal was filtered with a band-pass 730AF30 filter (30 nm band cut centred at 730 nm), placed in front of a NIR-sensitive CCD camera (Hamamatsu ORCA AG) mounted with a f/15-mm objective (Schneider Kreutznach). For all mice, a 2 cm² rectangle area on the head was scanned and a dedicated algorithm generated a 3D reconstruction of the NIR signal distribution in the head[43]. The total NIR signal within the reconstructed volume (arbitrary units) was quantified for all mice.

Mice were then imaged—live animals and brains that had been removed after the mice were killed—using Fluobeam800 (Fluoptics, France) ($\lambda_{exc} = 780$ nm, $\lambda_{em} > 820$ nm; 500 ms exposure time). The irradiance on the imaging field was 10 mW cm⁻². Note that for both imaging systems exposure times may vary from 100 ms to 10 s. These combinations of power and exposure times correspond to a maximum energy of 140 mJ cm⁻², which is far lower than the maximum permissible exposure limit for skin at these wavelengths (2 J cm⁻²). For each individual, a region of interest was defined manually. Two analysis methods were used to quantify the grey level variations within each region of interest. The first analysis corresponds to the local standard deviation between a given pixel and its neighbouring pixels delimited by a circular region of a given radius (here $r = 3$). For each individual, the average value of these standard deviations was calculated within the MLSD. The second analysis corresponds to the MG measurement. The gradient is conventionally estimated by convolution with the partial derivatives of a Gaussian kernel parameterized with $\sigma = 1$.

For ex vivo fluorescence microscopy, mice were euthanized and their brains removed, coronal slices were cut using a brain matrix (1.0 mm, Stoelting, USA) and mounted between the slide and coverslip. Macroscopic fluorescence imaging was performed with a MacroFluo (Z16 APO, Leica, Germany) fluorescence stereomicroscope, equipped with a highly sensitive CCD camera (iKon-M, Andor, Northern Ireland) with a 515–560 nm excitation and a 590 nm long-pass emission filter. Images were acquired with an objective ×0.8 at ×2.5 magnification.

Reporting Summary. Further information on research design is available in the Nature Research Reporting Summary linked to this article.

Data availability

The data that support the plots within this paper and other findings of this study are available from the corresponding author upon reasonable request.

References

50. Plissonneau, M. et al. Gd-nanoparticles functionalization with specific peptides for ß-amyloid plaques targeting. *J. Nanobiotechnol.* **14**, 60 (2016).
51. Pansieri, J. et al. Mass and charge distributions of amyloid fibers involved in neurodegenerative diseases: mapping heterogeneity and polymorphism. *Chem. Sci.* **9**, 2791–2796 (2018).
52. Sulatskaya, A. I., Rodina, N. P., Povarova, O. I., Kuznetsova, I. M. & Turoverov, K. K. Different conditions of fibrillogenesis cause polymorphism of lysozyme amyloid fibrils. *J. Mol. Struct.* **1140**, 52–58 (2017).
53. Kavanagh, G. M., Clark, A. H. & Ross-Murphy, S. B. Heat-induced gelation of globular proteins: part 3. molecular studies on low pH β-lactoglobulin gels. *Int. J. Biol. Macromol.* **28**, 41–50 (2000).
54. Lembré, P., Martino, P. D. & Vendrely, C. Amyloid peptides derived from CsgA and FapC modify the viscoelastic properties of biofilm model matrices. *Biofouling* **30**, 415–426 (2014).
55. Peng, H., Ruan, Z., Long, F., Simpson, J. H. & Myers, E. W. V3D enables real-time 3D visualization and quantitative analysis of large-scale biological image data sets. *Nat. Biotechnol.* **28**, 348–353 (2010).
56. Peng, H., Bria, A., Zhou, Z., Iannello, G. & Long, F. Extensible visualization and analysis for multidimensional images using Vaa3D. *Nat. Protoc.* **9**, 193–208 (2014).
57. Peng, H. et al. Virtual finger boosts three-dimensional imaging and microsurgery as well as terabyte volume image visualization and analysis. *Nat. Commun.* **5**, 4342 (2014).

nature research

Corresponding author(s): Dr. Vincent Forge

Last updated by author(s): Mar 21, 2019

Reporting Summary

Nature Research wishes to improve the reproducibility of the work that we publish. This form provides structure for consistency and transparency in reporting. For further information on Nature Research policies, see Authors & Referees and the Editorial Policy Checklist.

Statistics

For all statistical analyses, confirm that the following items are present in the figure legend, table legend, main text, or Methods section.

n/a	Confirmed	
☐	☒	The exact sample size (*n*) for each experimental group/condition, given as a discrete number and unit of measurement
☐	☒	A statement on whether measurements were taken from distinct samples or whether the same sample was measured repeatedly
☐	☒	The statistical test(s) used AND whether they are one- or two-sided *Only common tests should be described solely by name; describe more complex techniques in the Methods section.*
☐	☒	A description of all covariates tested
☐	☒	A description of any assumptions or corrections, such as tests of normality and adjustment for multiple comparisons
☐	☒	A full description of the statistical parameters including central tendency (e.g. means) or other basic estimates (e.g. regression coefficient) AND variation (e.g. standard deviation) or associated estimates of uncertainty (e.g. confidence intervals)
☐	☒	For null hypothesis testing, the test statistic (e.g. *F*, *t*, *r*) with confidence intervals, effect sizes, degrees of freedom and *P* value noted *Give P values as exact values whenever suitable.*
☐	☒	For Bayesian analysis, information on the choice of priors and Markov chain Monte Carlo settings
☐	☒	For hierarchical and complex designs, identification of the appropriate level for tests and full reporting of outcomes
☐	☒	Estimates of effect sizes (e.g. Cohen's *d*, Pearson's *r*), indicating how they were calculated

Our web collection on statistics for biologists contains articles on many of the points above.

Software and code

Policy information about availability of computer code

Data collection	See the Methods section for details. Data Station (v2.7), Decay Analysis (v6.8) from Horiba Scientific, Carl Zeiss Zen software, Image J (v1.50), Microsoft Excel, Sigma Plot, Vaa3D.
Data analysis	See the Methods section for details. Data Station (v2.7), Decay Analysis (v6.8) from Horiba Scientific, Carl Zeiss Zen software, Image J (v1.50), Microsoft Excel, Sigma Plot, Vaa3D.

For manuscripts utilizing custom algorithms or software that are central to the research but not yet described in published literature, software must be made available to editors/reviewers. We strongly encourage code deposition in a community repository (e.g. GitHub). See the Nature Research guidelines for submitting code & software for further information.

Data

Policy information about availability of data

All manuscripts must include a data availability statement. This statement should provide the following information, where applicable:

- Accession codes, unique identifiers, or web links for publicly available datasets
- A list of figures that have associated raw data
- A description of any restrictions on data availability

The data that support the findings of this study are available from the corresponding author upon reasonable request.

Field-specific reporting

Please select the one below that is the best fit for your research. If you are not sure, read the appropriate sections before making your selection.

☒ Life sciences   ☐ Behavioural & social sciences   ☐ Ecological, evolutionary & environmental sciences

Life sciences study design

All studies must disclose on these points even when the disclosure is negative.

Sample size	Eleven mice per group were used in each experiment. Sample size was determined to be adequate based on the magnitude and consistency of measurable differences between groups as a proof of concept.
Data exclusions	No data were excluded.
Replication	All attempts at replication were successful.
Randomization	We did not use randomization to assign animals to experimental groups, and all informations about models and groups are included in the Methods section.
Blinding	Data collection and analysis followed exactly the same systematic protocols. Investigators were not blinded to group allocation during experiments. All informations are included in the Methods section.

Reporting for specific materials, systems and methods

We require information from authors about some types of materials, experimental systems and methods used in many studies. Here, indicate whether each material, system or method listed is relevant to your study. If you are not sure if a list item applies to your research, read the appropriate section before selecting a response.

Materials & experimental systems

n/a	Involved in the study
☒	☐ Antibodies
☒	☐ Eukaryotic cell lines
☒	☐ Palaeontology
☐	☒ Animals and other organisms
☒	☐ Human research participants
☒	☐ Clinical data

Methods

n/a	Involved in the study
☒	☐ ChIP-seq
☒	☐ Flow cytometry
☒	☐ MRI-based neuroimaging

Animals and other organisms

Policy information about studies involving animals; ARRIVE guidelines recommended for reporting animal research

Laboratory animals	Female APPswe/PSEN1dE9 and C57/Bl6 mice (n=11 per group) of 18.4 +/- 2.6 months were used in accordance with the European Economic Community guideline and the "Principles of Laboratory Animal Care" (NIH publication N 86-23 revised 1985). For more informations, informations are available in Methods section.
Wild animals	This study did not involved wild animals.
Field-collected samples	This study did not involved samples from the field.
Ethics oversight	The protocols were approved by an animal ethics committee and received the authorization of the French Ministry of Higher Education and Research (authorization #8854-2017031314338357).

Note that full information on the approval of the study protocol must also be provided in the manuscript.